RSC Advances

PAPER

View Article Online
View Journal | View Issue

Open Access Article. Published on 15 December 2021. Downloaded on 5/22/2026 10:09:20 AM.
This article is licensed under a Creative Commons Attribution-NonCommercial 3.0 Unported Licence.

Check for updates

Cite this: *RSC Adv.*, 2021, **11**, 39966

Co nanoparticles decorated with N-doped carbon nanotubes as high-efficiency catalysts with intrinsic oxidase-like property for colorimetric sensing†

Tao Chen, Jinmin Cao, Xiaofang Bao, Yu Peng, Li Liu * and Wensheng Fu*

Artificial nanozymes are designed for pursuing the functions of splendid catalytic efficiency and prominent selectivity of natural enzymes, meanwhile obtaining higher stability than that of natural enzymes. This emerging technology shows widespread application in the crossing field between nanotechnology and biomedicine. In this work, we employed a universal approach to fabricate a Co@N-CNTs hybrid nanocomposite as an oxidase mimic, in which fine Co nanoparticles were wrapped in N-doped carbon nanotubes, stacking on a hollow dodecahedron carbon skeleton. The synergistic effects of nanostructure engineering, N-doping and carbon coating, as well as the derived interfacial effect contribute to the glorious oxidase-like activity, stability and reusability. It can catalytically oxidize the colorless substrate 3,3′,5,5′-tetramethylbenzidine (TMB) to a blue oxidation product (ox-TMB). As a result, a colorimetric technique with excellent selectivity and sensitivity for detecting ascorbic acid (AA) with naked eyes was established, in view of specific inhibitory effects towards oxidation of TMB. Under optimal detection conditions, this method exhibits a good linearity ranging from 0.1 to 160 μM with a low limit of detection (LOD) of 0.076 μM. For practical applications, Co@N-CNTs hybrid catalyst as a mimic oxidase was used for the determination of AA in human serum, which yielded satisfactory results. This work may serve as a new research thought to guide the design of high-performance nanozymes and establish a sensing platform for the detection of AA.

Received 24th October 2021
Accepted 9th November 2021

DOI: 10.1039/d1ra07849f

rsc.li/rsc-advances

1. Introduction

Natural enzymes exist widely in organisms and play a crucial role in regulating biological functions owing to their high catalytic activity and substrate specificity.[1,2] Although promising, their applications in *in vitro* reactions are usually impeded by the high price, low stability, strong pH dependency and inferior reusability.[3] Compared with the natural enzymes, artificial enzymes with the advantages of low price, desirable catalytic activity, convenient preparation and excellent resistance to harsh environmental conditions are widely used in biosensing, biological pharmacy, biological molecular detection, material separation, and chemical catalysis.[4] With the development of the study on mimic enzymes, the application of various mimic materials, especially peroxide mimic enzymes, has been very mature. As is known to all, H_2O_2 is needed to explore the peroxidase-like activity. However, the presence of H_2O_2 will not only destroy the structure of the organic substrate in the reaction system, but also cause secondary pollution due to the difficulty in recovery.[5,6] Therefore, without the use of H_2O_2, it is of greater research value to construct a simple detection platform using an oxidase-like enzyme.

At present, many noble metal nanomaterials have been proved to possess mimic oxide enzyme properties. For example, Naoki Toshima *et al.* proposed a method of loading gold nanoparticles on platinum nanoclusters forming a complex, which exhibited a conspicuous activity for the catalytic oxidation of glucose.[7] Regrettably, the application of these noble metal nanomaterials is limited by their high cost and low abundance. Therefore, the cost-effective and easily accessible transition metal nanomaterials with the oxidase-like activity deserve to be more explored. Transition metal cobalt, due to its unique electronic structure of $3d^74s^2$, has raised great concern in the area of nanoenzymes, especially cobalt particles in nanoscale may act as splendid oxidase-like enzymes.[8] However, the nanosized metal particles are thermodynamically unstable when directly exposed to the reaction solution, considering the fact that the high surface energy easily leads to agglomeration and inactivation.[3,9] As such, a method of coating metal nanoparticles with other materials is urgently required to make them relatively stable under traditional reaction conditions.

Chongqing Key Laboratory of Green Synthesis and Applications, College of Chemistry, Chongqing Normal University, Chongqing 401331, China. E-mail: liliu1208@163.com; fuwensheng@cqnu.edu.cn

† Electronic supplementary information (ESI) available. See DOI: 10.1039/d1ra07849f

© 2021 The Author(s). Published by the Royal Society of Chemistry

Open Access Article. Published on 15 December 2021. Downloaded on 5/22/2026 10:09:20 AM.
This article is licensed under a Creative Commons Attribution-NonCommercial 3.0 Unported Licence.

Recently, loading nanozymes onto carbonaceous supports such as carbon nanotubes,[10] graphenes,[11] and porous carbon[12] is deemed as an effective strategy to prevent aggregation and ameliorate the catalytic activity of nanozymes. In particular, carbon nanotubes (CNTs) with porous structures can provide high specific surface area, admirable conductivity, desirable chemical stability and biocompatibility, which have a good ability to regulate the rapid electron transfer kinetics.[13] However, the catalytic activity of carbon nanotubes is finite. Studies show that non-metallic dopants such as nitrogen, oxygen, boron, sulfur and phosphorus can observably enhance the oxidase-like catalytic activity of carbon materials.[14,15] Among these, more electronegative nitrogen is an effective dopant, which can regulate the charge distribution on the surface of carbon materials and provide a large number of structural defects.[16] Meanwhile, the lone-pair electrons on N atoms are conducive to anchoring the transition metal nanoparticles *via* coordination interaction. For example, Liu's group synthesized Co–N–C composites immobilized on N-doped carbon nanotubes for the catalytic oxidation of ethylbenzene. As the introduction of N heteroatoms and combination of CNTs promote the mass transfer between O_2 and the substrate active site, the selectively catalytic oxidation performance of Co-N-Cx/CNTs for ethylbenzene was significantly improved.[17]

In addition, designing the novel morphology by nanostructure engineering is also a valid strategy to obtain artificial nanoenzymes with prominent catalytic activity, because the unique micro-structure could endow a large specific surface area and contribute to the rapid transfer of catalytic reaction-related species. For instance, Zhuang, *et al.* synthesized a hollow Co_3O_4@CuO nanocage, which presents high oxidase-like properties and is applied for dopamine biomolecular detection.[18] Moreover, according to Chen's report, a Pt-loaded hollow mesoporous carbon nanosphere is proposed as the peroxidase mimic, which offers a huge hollow cavity and a mesoporous carbon skeleton.[3] Its excellent peroxidase-like catalytic activity is ascribed to the unique hollow structure and the interfacial effect between metal Pt nanoparticles and the carbon skeleton; consequently, it could be applied in the colorimetric detection of ascorbic acid. Given the above, it is still a great challenge to construct hybrid nanomaterials with oxidase-mimic performance by combination of nanostructure engineering, element doping and loading of carbon materials.

Ascorbic acid (AA) is an important and special water-soluble vitamin. Its molecular structure is very simple, while the physical and chemical properties are unstable.[19] The human body requires AA for certain functions to maintain the normal function of the human body. Due to AA deficiency, the synthesis of collagen will be affected, resulting in a cell connection barrier, meanwhile causing scurvy leading to decreased human immunity and body's emergency capacity.[20] Therefore, it is very critical to precisely detect AA in food products and pharmaceutical formulation and for disease diagnosis. To date, various methods such as electrochemical methods,[21] fluorescence spectroscopy,[22] liquid chromatography,[23] and chemiluminescence[24] have been exploited for AA detection. Admittedly, these platforms enable the detection of AA with excellent sensitivities; however, there still exist some limitations, for example, they are time-consuming and these detection methods often demand complex detectors or operation. By contrast, the colorimetric assay has obvious advantages including simple operation, rapid response and easy readout with the naked eye, which is urgently needed for AA detection.

In this work, we synthesized a Co@N-CNTs hybrid nanomaterial by combination of nanostructural engineering, element doping and loading of carbon materials, in which Co nanoparticles were loaded on N-doped carbon nanotubes assembled in a hollow rhomboid dodecahedron framework. The hollow microstructure with open transfer channels contributes to the more exposed active sites and improves the molecular diffusion kinetics. Besides, coating N-doped carbon nanotubes (N-CNTs) onto Co nanoparticles endows them with good electron conductivity and prevents aggregation. Meanwhile, the hybrid structure creates a heterojunction at the junction between Co nanoparticles and N-CNTs, leading to an interfacial electric field, which further expedites the electron transfer. In addition, doping N atoms into a carbon skeleton could effectively create positive charge sites on nearby carbon atoms ($C^{\delta+}$), which is beneficial to adsorb dissolved oxygen onto the surface of the Co@N-CNTs catalyst, and then the adsorbed O_2 is transferred to the catalytic active sites (pyridinic N–Co and pyrrolic N–Co sites) to disintegrate into ROS species, promoting the oxidation of the TMB substrate. Therefore, the synergistic catalytic effect endows the Co@N-CNTs hybrid nanomaterial with outstanding oxidase-like activity, which enables to catalyze the oxidation of the TMB substrate to produce blue oxidation products. As a result, a colorimetric detection platform against ascorbic acid with bare eyes was established based on the oxidase-like activity of the Co@N-CNTs mimic enzyme and the inhibitory effect induced by AA. Considering the sensitivity, selectivity and long storage stability, the Co@N-CNTs catalyst shows great potential in the detection of AA in practical applications.

2. Results and discussion

2.1 Synthesis and characterization of the Co@N-CNTs catalyst

The synthesis procedure of hollow Co@N-CNTs hybrid dodecahedron frameworks is exhibited in Fig. 1. First, solid ZIF-8 dodecahedrons as precursors with smooth surface and uniform size distribution were synthesized, as shown in Fig. S1a and b.† Then, considering the similar topological structure and cell parameters of ZIF-8 ($a = b = c = 16.9910$ Å)[25] and ZIF-67 ($a = b = c = 16.9589$ Å),[26] ZIF-67 was epitaxially grown on the surface of the ZIF-8 dodecahedron to form a core–shell ZIF-8@ZIF-67 intermediate, which was identified by X-ray diffraction (XRD) (Fig. S1c†). Scanning electron microscopic (SEM) image in Fig. S1d† verifies no changes in the morphology except for the slight increase in size. Finally, the core–shell ZIF-8@ZIF-67 intermediate was *in situ* carbonized and doped to transform into a hollow Co@N-CNTs hybrid dodecahedron framework through the pyrolysis treatment of ZIF-8@ZIF-67 at 900 °C under the flow of N_2. Under the high-temperature condition, Zn

Open Access Article. Published on 15 December 2021. Downloaded on 5/22/2026 10:09:20 AM.
This article is licensed under a Creative Commons Attribution-NonCommercial 3.0 Unported Licence.

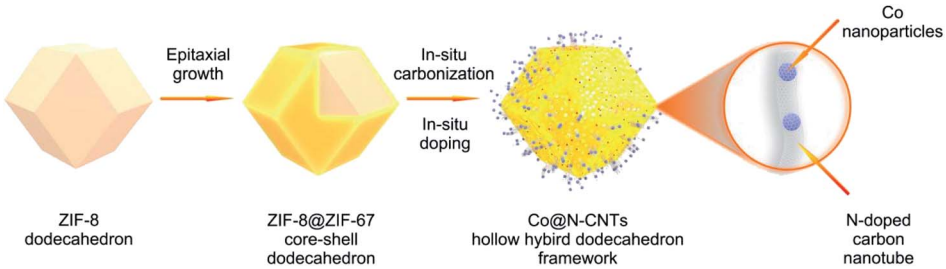

Fig. 1 Schematic of the synthesis procedure for Co@N-CNTs hollow hybrid dodecahedron frameworks.

atoms were evaporated to produce a lot of pores, and the nitrogenous imidazole ligands of internal ZIF-8 core were decomposed into an *in situ* N-doped hollow dodecahedron carbon framework. Meanwhile, Co^{2+} ions in the ZIF-67 shell were reduced to Co nanoparticles under the action of C–H bonds and carbon materials. Of note, the imidazole organic ligands of the external ZIF-67 shell were also *in situ* carbonized and doped to form N-doped carbon materials. By controlling the thickness of the ZIF-67 shell, some locally incomplete N-doped carbon fragments were obtained after the pyrolysis process, which were anchored onto the surface of the dodecahedron carbon framework derived from the internal ZIF-8 core. To reduce the thermodynamic surface energy, the above N-doped carbon fragments were further curled up into the N-doped multiwall carbon nanotubes, meanwhile trapping the adjacent Co nanoparticles. Ultimately, the Co@N-CNTs hybrid catalyst with a special morphology of Co nanoparticles wrapped in N-doped carbon nanotubes anchoring on a hollow dodecahedron framework was successfully obtained.

As displayed in Fig. 2a, Co@N-CNTs dodecahedron is successfully acquired on a large scale, revealing the feasibility of the synthetic method. The enlarged SEM image in Fig. 2b exhibits that Co@N-CNTs inherits the dodecahedron morphology of the precursor, but the surface becomes rougher along with slight shrinkage. This observation indirectly confirms the mass loss during pyrolysis. Fig. 2c shows the transmission electron microscopic (TEM) image of the Co@N-CNTs dodecahedron, in which the hollow structure is clearly observed. In addition, its surface seems to be decorated with many nanoparticles (Fig. 2d). Zooming in further would show that these nanoparticles with an average size of ~10 nm are wrapped in well-organized nanotubes, and the nanotubes are mounted on the hollow dodecahedron framework, as shown in Fig. 2e. Meanwhile, a lot of holes can be observed in the dodecahedron framework, as marked by yellow circles in Fig. 2e, implying that the material owns a considerable surface area. In order to verify this point, the Brunauer–Emmett–Teller (BET) measurement was adopted. As illustrated in Fig. S2,† the N_2 adsorption–desorption isotherm of the Co@N-CNTs dodecahedron displays the characteristic behavior of type IV with a distinct hysteresis loop, manifesting the porous structure. In addition, the pore size distribution curve (inset) shows that the size of pores is mainly concentrated at 4.04 nm, illustrating the existence of mesoporous. Additionally, the specific surface area determined from the BET model reaches up to 407.71 $m^2\ g^{-1}$ with a pore volume of 0.48 $cm^3\ g^{-1}$. Such a mesoporous structure with a huge specific surface area is conducive to the diffusion of reactants and the exposure of active sites, contributing to a desired catalytic activity.

What is more, the HRTEM (Fig. 2f) image shows a typical lattice fringe with a spacing of ~0.206 nm corresponding to the (111) lattice planes of metallic Co. A few lattice fringes with a spacing of ~0.338 nm are also detected at the edge of the nanoparticles, which are ascribed to the (002) lattice plane of graphitized carbon. The thickness of the carbon shell is 2–4 nm. Besides, the SAED image (inset) reveals the polycrystalline nature. The X-ray diffraction (XRD) measurement was utilized to further confirm the crystalline feature and chemical component of the Co@N-CNTs dodecahedron. In Fig. 2g, the XRD pattern displays three diffraction peaks located at 44.3°, 51.5°, and 75.9° corresponding to the (111), (200), and (220) facets of face-centered cubic (fcc) Co (PDF no. 01-1255). Interestingly, the diffraction peak (~26°) of graphitized carbon is not found in the XRD pattern, but the characteristic spectral lines of two sequence regions of carbon materials appear in the Raman spectrum (Fig. S3†). This phenomenon suggests the poor crystalline nature of graphitized carbon in the Co@N-CNTs material. In Raman spectrum, two characteristic spectral lines representing different chemical structures appear in the first frequency of 1100–1800 cm^{-1}, and the 2D band with a frequency dependent on laser excitation energy appears in the second frequency of 2400–3000 cm^{-1}. There exists a D band for the A_{1g} vibration mode located at 1360 cm^{-1}, showing the presence of disordered carbon in the Co@N-CNTs structure. In addition, the characteristic G band at *ca.* 1583 cm^{-1} reflects the in-plane vibration of sp^2 carbon with a high degree of graphitization. As it is well known, the different half-peak width and relative intensity of G and 2D peaks can reflect the interaction between multiple graphite layers.[27] The relative strength of the 2D band at 2700 cm^{-1} is weaker than that of the G band, and the peak of the 2D band is obviously wider. This result indicates that multi-layer graphitized carbon was obtained by calcination of carbonaceous organic ligands at high temperatures. Besides, the ratio of I_D/I_G was determined to be 1.14, indicating a lot of structural defects in the carbon materials, which could provide plentiful active sites for the catalytic reaction.

The energy-dispersive X-ray spectroscopy (EDX) coupling with high-angel annular dark-field scanning transmission

 © 2021 The Author(s). Published by the Royal Society of Chemistry

Open Access Article. Published on 15 December 2021. Downloaded on 5/22/2026 10:09:20 AM.
This article is licensed under a Creative Commons Attribution-NonCommercial 3.0 Unported Licence.

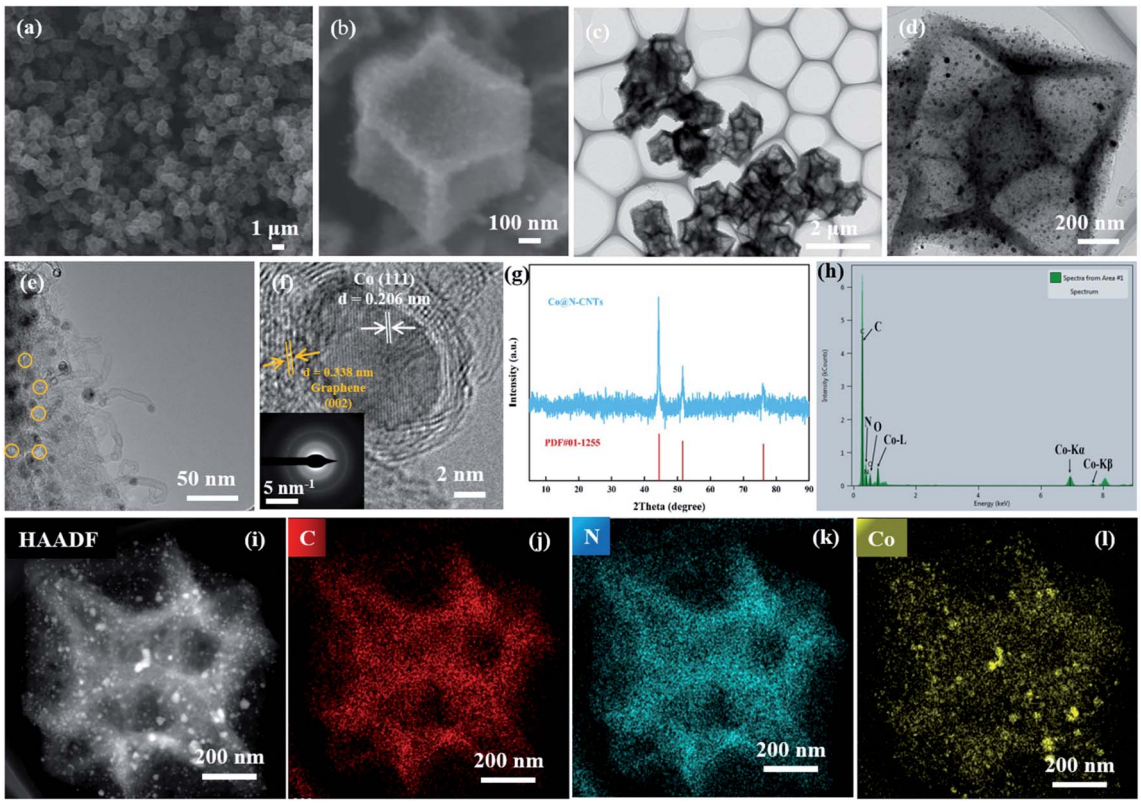

Fig. 2 (a and b) SEM images, (c–e) the stepwise magnified TEM images, (f) HRTEM image (inset is the SAED pattern), (g) XRD pattern, (h) EDX spectrum, (i) HAADF-STEM image and (j–l) EDX elemental mapping images of the Co@N-CNTs hollow hybrid dodecahedron framework.

electron microscopy (HAADF-STEM) were also employed to characterize the microstructure and elemental distribution in the Co@N-CNTs dodecahedron. The result shown in Fig. 2h indicates that the C, N, O and Co elements exist in the Co@N-CNTs material, wherein the O element may come from the oxidation of surface. The elemental mapping images in Fig. 2i–l show that C and N elements evenly distribute throughout the region of dodecahedron, while the Co element only disperses on the region of nanoparticles, further testifying the novel structure that Co nanoparticles were wrapped in N-doped carbon nanotubes assembled in a hollow dodecahedron framework.

In order to further investigate the surface chemical components and chemical states of the Co@N-CNTs, the X-ray photoelectron spectroscopy (XPS)[28,29] measurement was carried out. The survey-scan XPS spectrum of Co@N-CNTs (Fig. S4a†) exhibits the presence of C, N, Co and O elements. The asymmetrical C 1s spectrum in Fig. 3a is made up of three types of bonds, which are assigned to C–O at 288.6 eV, C–N at 285.9 eV, C–C or C=C at 284.8 eV.[16] In addition, three N types could be distinguished from the N 1s spectrum (Fig. 3b), including graphite N at 401.8 eV, pyrrolic N at 400.9 eV and pyridinic N at 398.8 eV.[30] Pyridinic N and pyrrolic N usually act as metal-coordination sites due to the lone-pair electrons.[31] Thus, they may serve as catalytic active sites to produce ROS, enhancing enzyme-like activities. This result confirms that N atoms are successfully doped into carbon materials after the high-temperature pyrolysis process. More importantly, owing to higher electronegativity, doping N atoms into a carbon skeleton could induce positive charge sites of adjacent carbon atoms. To confirm the positive charge sites of carbon atoms nearby N atoms in Co@N-CNTs, we prepared the Co@C composite and compared the C 1s XPS spectrum. As displayed in Fig. S4b,† it is not difficult to find that the C 1s XPS peak in the Co@N-CNTs is positively shifted (0.2 eV) compared to that in Co@C, indicating that the small electron density transfers from C atoms to N atoms. This observation proves that N-doping brings about the electron delocalization in the doped region. Therefore, the C and N atoms in the Co/N-CNTs nanozyme have partial positive charge ($C^{\delta+}$) and negative charge ($N^{\delta-}$). The positive charge sites on nearby carbon atoms ($C^{\delta+}$) are beneficial to adsorb dissolved oxygen onto the surface of the Co@N-CNTs catalyst, thus promoting the oxidase-like activity. The Co 2p spectrum is illustrated in Fig. 3c, which is deconvoluted into four components. The fitting peaks at 795.4 and 778.6 eV are assigned to the binding energy of Co in a zero valence state. In addition, the XPS peaks at 796.7 and 780.4 eV are consistent with the Co(II) valence state, corresponding to the binding energy of CoO.[32,33] Notably, unlike the XRD data, in which only metallic Co was identified, the presence of the Co–O peak in the XPS spectrum signifies that metal Co nanoparticles are susceptible to inevitable surface oxidation to form amorphous cobalt oxides.[34] Besides, the satellite is located at 803.4 eV and 786.3 eV, and the Co–N_x peak is situated at 782.5 eV.[35] The O 1s spectrum (Fig. 2d) exhibits three characteristic peaks corresponding to

Open Access Article. Published on 15 December 2021. Downloaded on 5/22/2026 10:09:20 AM.
This article is licensed under a Creative Commons Attribution-NonCommercial 3.0 Unported Licence.

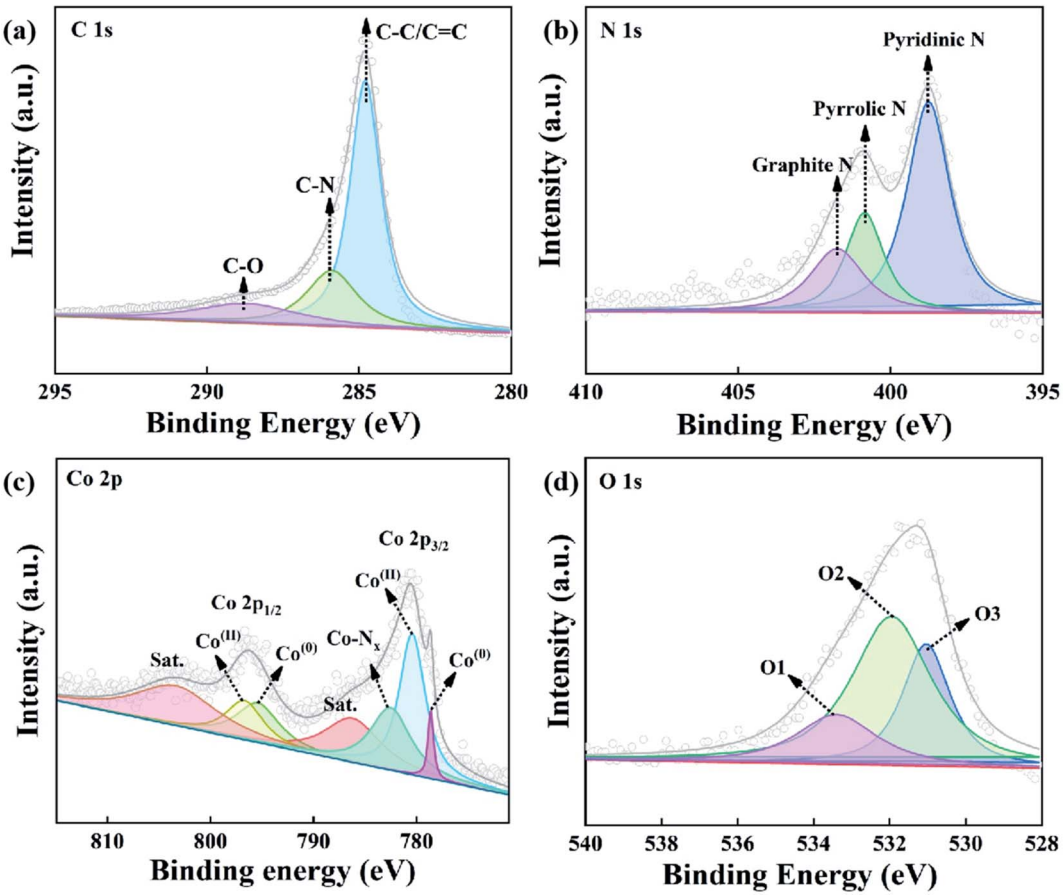

Fig. 3 High-resolution XPS spectrum of (a) C 1s, (b) N 1s, (c) Co 2p and (d) O 1s in the Co@N-CNTs hollow hybrid dodecahedron framework, respectively.

physisorbed-/chemisorbed water on the surface of the Co@N-CNTs material (O1 at 533.4 eV), the dissociative O_2 adsorption on coordinatively unsaturated metal atoms (O2 at 532.0 eV), and the typical M–O bond derived from the inevitable surface oxidation (O3 at 531.0 eV). This result further verifies that the material may suffer from slight surface oxidation, in accordance with the observations in the Co 2p spectrum and EDX data. In combination with the TEM, XRD, EDX and XPS analysis, it is not difficult to conclude the successful preparation of the Co@N-CNTs dodecahedron.

2.2 Exploring the oxidase-like properties of Co@N-CNTs

Most of the currently developed mimic enzymes usually use H_2O_2 as an oxidant, which severely hinders their biological applications. Consequently, the mimic oxide enzyme shows more universal bio-application, for the reason that it can employ ambient oxygen as an electron acceptor to oxidize the substrate under the reaction condition without H_2O_2. To evaluate the oxidase-like property of the Co@N-CNTs dodecahedron, we adopted 3,3′,5,5′-tetramethylbenzidine (TMB) as the allochroic substrate and monitored the oxidation of the TMB process *via* a colorimetric method as well as UV-vis measurement. As exhibited in Fig. 4a, an obvious absorption peak at 652 nm is detected when both the Co@N-CNTs catalyst and the TMB substrate co-exist in an acetate buffer solution, accompanied by a color change from colorless to blue. However, the system without the Co@N-CNTs catalyst or TMB presents no obvious color change. This observation illustrates that Co@N-CNTs can rapidly catalyze the oxidation of TMB to form the blue oxidation state of TMB ($oxTMB^+$), displaying the excellent oxidase-like activity. In order to emphasize the component and structural advantages of Co@N-CNTs dodecahedron, two contrast materials were also prepared (see Fig. S5 and S6†). Then, their oxidase-like activity was also tested under the same conditions with TMB as the substrate. As exhibited in Fig. S7,† the Co@N-CNTs catalyst presents optimal oxidase-like activity, compared with Co_3O_4@N-CNTs and N-CNTs catalysts. Moreover, the absorption peak at 652 nm increases gradually over time; meanwhile, the color of the solution becomes increasingly obvious (Fig. 4b). Notably, the absorbance also rises with the increase in the concentration of the Co@N-CNTs catalyst or TMB substrate (Fig. 4c and d), indicating the fast reaction rate.

Similar to natural enzymes, the catalytic performance of the mimic enzyme also follows a factor-dependent manner, which is closely related to the temperature, concentration, pH value and reaction time. Accordingly, we explored the influence of the four factors on the oxidase-like activity of the Co@N-CNTs catalyst. It is not hard to find that the absorbance at 652 nm

 © 2021 The Author(s). Published by the Royal Society of Chemistry

Open Access Article. Published on 15 December 2021. Downloaded on 5/22/2026 10:09:20 AM.
This article is licensed under a Creative Commons Attribution-NonCommercial 3.0 Unported Licence.

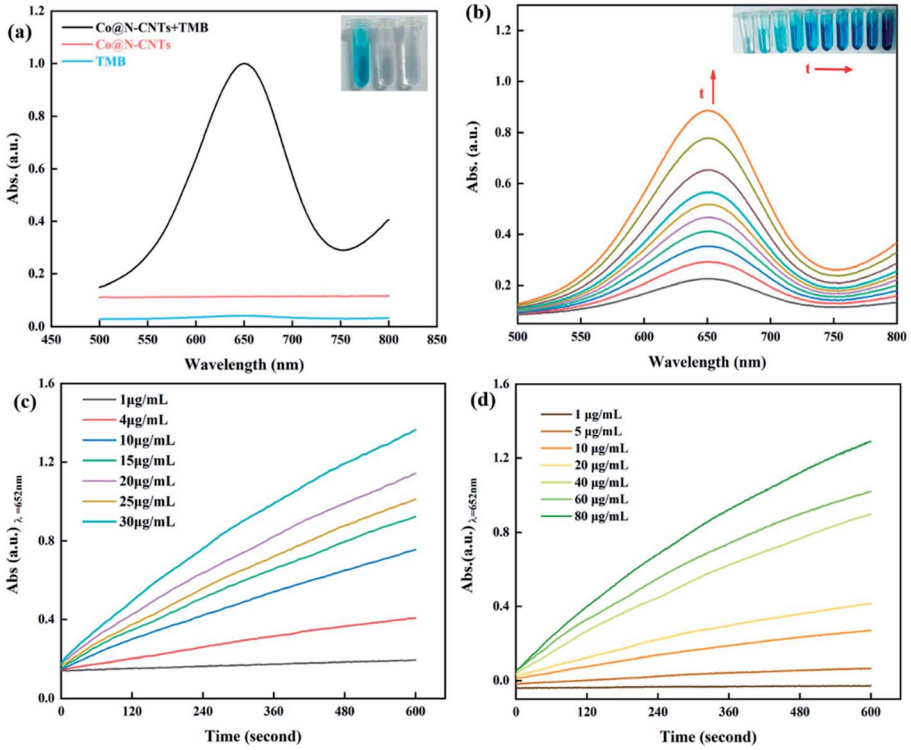

Fig. 4 (a) UV-vis absorption spectra of varied reaction systems in an acetate buffer solution (pH = 4.0) recorded at 10 min (the inset is their corresponding photograph). (b) UV-vis absorption spectra over time in the presence of 80 μg mL^{-1} TMB and 10 μg mL^{-1} Co@N-CNTs, within 10 minutes (the inset displays the color changes of the reaction solution with time). (c and d) Time-dependent absorbance at 652 nm with different concentrations of the Co@N-CNTs catalyst in the presence of 80 μg mL^{-1} TMB (c) and different concentrations of TMB in the presence of 10 μg mL^{-1} Co@N-CNTs (d).

fluctuates with the change in pH (2.4–6.0) and reaches the optimal value at pH = 4.0 (Fig. S8a and b†). The catalytic activity decreases sharply when the pH exceeds 4.8, owing to the poor solubility of the diamine structure of TMB under high pH conditions. Besides, in Fig. S8c and d,† the Co@N-CNTs catalyst exhibits an outstanding oxidase-like activity at a wide range of temperatures (25–60 °C). As we all know, natural enzymes can only perform the catalytic function within a limited temperature range in consideration of molecular stability; however, the Co@N-CNTs catalyst can operate under extreme conditions of temperature. For an easy operation, room temperature (~25 °C) was selected as the test temperature. According to Fig. S8e and f,† the catalytic activity increases significantly with the increase in TMB concentration, when the TMB concentration is lower than 80 μg mL^{-1}. However, the catalytic activity increases slowly when the TMB concentration is above 80 μg mL^{-1}. Therefore, 80 μg mL^{-1} is deemed as the optimum TMB concentration. Similarly, the absorption values at 652 nm are positively correlated with the concentration of the catalyst (Fig. S8g and h†). In order to guarantee the accuracy of measurements, the absorption value should be kept at 1.2, thereby the optimized concentration of the Co@N-CNTs catalyst was determined to be 10 μg mL^{-1}. In addition, as demonstrated in Fig. S8i and j,† the catalytic reaction was completed within 10 min (Fig. S8i and j†). Consequently, optimal conditions (pH = 4.0, T = 25 °C, C_{TMB} = 80 μg mL^{-1}, $C_{catalyst}$ = 10 μg mL^{-1} and T_{time} = 10 min) were selected for the subsequent analysis.

Considering the practical utilization, stability and reusability are the two important metrics to judge the performance of nanozymes. As revealed in Fig. S9a,† the oxidase-like activity of the Co@N-CNTs catalyst remains basically steady within 25 days of storage period, displaying the excellent long-term stability. Furthermore, taking the weight loss in each cycle into consideration, the absorbance declines slightly after five reuse cycles (Fig. S9b†). However, the oxidase-like activity still maintains over 70.6% of the initial activity. Additionally, the SEM image (Fig. S10†) of the Co@N-CNTs catalyst after the stability test displays no obvious change, essentially explaining the structural stability. The satisfactory stability and reusability of the Co@N-CNTs catalyst make it possible for long-term applications in the field of catalysis.

Following that, the oxidase-like behavior of the Co@N-CNTs catalyst is profoundly investigated through steady-state kinetic analysis. The typical Michaelis–Menten curve is plotted by monitoring the TMB concentration in a reasonable range (1–120 μg mL^{-1}) while maintaining the concentration of the catalyst at 10 μg mL^{-1} (Fig. 5a). Obviously, the reaction velocity is high at lower TMB concentrations while the reaction velocity does not proportionally increase with the TMB concentration at higher substrate concentrations demonstrating a saturation effect. The effect might be attributed to the occupancy of

Open Access Article. Published on 15 December 2021. Downloaded on 5/22/2026 10:09:20 AM.
This article is licensed under a Creative Commons Attribution-NonCommercial 3.0 Unported Licence.

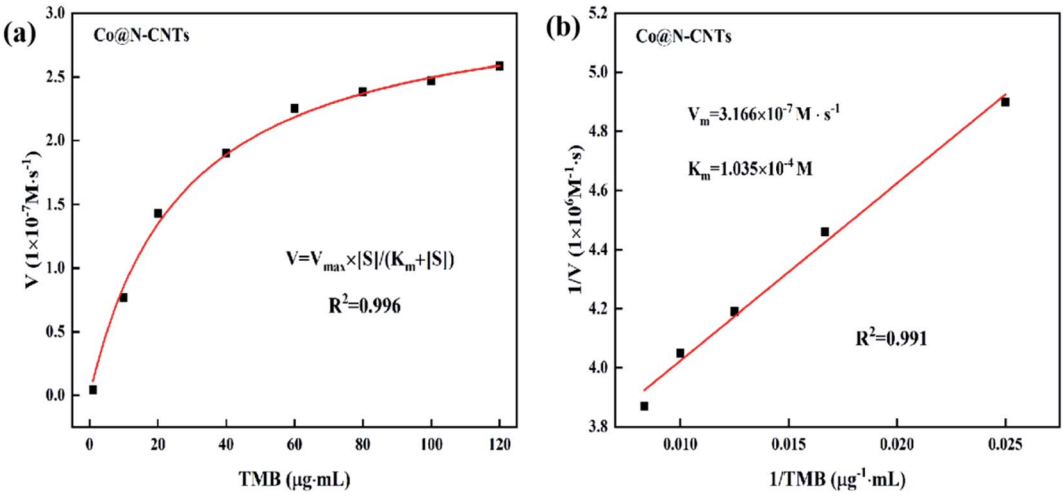

Fig. 5 Steady-state kinetic analysis of the Co@N-CNTs catalyst: (a) Michaelis–Menten curve and (b) Lineweaver–Burk plots of the TMB substrate for oxidase-like activity. The double reciprocal plot of TMB was made from the respective Michaelis–Menten curve.

catalytically active sites in the Co@N-CNTs catalyst by the substrate at higher TMB concentrations. The corresponding double-reciprocal Lineweaver–Burk plot was obtained, as shown in Fig. 5b and fitted to Michaelis–Menten equation:

$$V_0 = V_m[S]/(K_m + [S]) \quad (1)$$

wherein V_m is the maximum reaction rate, V_0 is the initial rate, [S] refers to the concentration of the TMB substrate, and K_m is the Michaelis constant. K_m and V_m are the indicators of the binding affinity and catalytic activity, respectively. The lower the K_m value, the stronger the affinity. In addition, the bigger the V_m value, the higher the catalytic activity.[36,37] The K_m value of Co@N-CNTs (1.035×10^{-4} M) for oxidase mimicking with TMB is lower than Co_3O_4@N-CNTs (1.613×10^{-4} M) and N-CNTs (1.688×10^{-4} M), indicating the better affinity of Co@N-CNTs towards TMB (Fig. S11†). Besides, the V_m value was calculated to be 3.166×10^{-7} M s^{-1}, which is much higher than that of Co_3O_4@N-CNTs (2.863×10^{-7} M s^{-1}), N-CNTs (1.673×10^{-7} M s^{-1}) and other mimic oxide enzymes reported in a recent work, as shown in Table S1.† It is reported in the literature that the negatively charged nanozymes often possess a stronger affinity towards TMB, as the amine groups of TMB carry the positive charges.[38] Therefore, to further illuminate such strong binding ability of Co@N-CNTs towards TMB, the zeta-potential (ζ) characterization was conducted (Fig. S12†). Obviously, comparing with Co_3O_4@N-CNTs (−3.35 mV) and N-CNTs (−1.88 mV), the Co@N-CNTs catalyst possesses the strongest negative charge (−6.11 mV), proving the contribution of electrostatic interaction toward the strong affinity.

To further figure out the possible reactive oxygen species (ROS) in the Co@N-CNTs catalytic system, several scavengers such as *p*-benzoquinone (PBQ), isopropanol (IPA) and tryptophan (TRP) were chosen as the free radical quenchers for probing superoxide anions ($O_2^{\bullet-}$), hydroxyl radicals ($^{\bullet}OH$) and singlet oxygen ($^1O_2$), respectively.[39] As revealed in Fig. 6a, the absorbance of the system with TRP is nearly the same with the blank control group. However, the oxidase-like activity of the Co@N-CNTs catalyst was dramatically decreased when the PBQ exists in the system. In addition, the catalytic activity was also slightly confined by introducing the IPA scavenger. Those results confirm the generation of $O_2^{\bullet-}$ accompanied by small doses of $^{\bullet}OH$, in the oxide-mimicking catalytic process of Co@N-CNTs. In parallel, the electron paramagnetic resonance (EPR) spectrum in Fig. 6b provides with a similar conclusion. The EPR technique would probe the generation of ROS using 5,5-dimethyl-1-pyridine *N*-oxide (DMPO) as a spin trapping reagent. Six characteristic peaks for $O_2^{\bullet-}$ adducts[40] and four characteristic quarter peaks for $^{\bullet}OH$ adducts[41] were distinctly observed, further disclosing the production of $O_2^{\bullet-}$ and $^{\bullet}OH$ in the catalytic reaction solution.

To elucidate the role of O_2 in the catalytic reaction, the oxidase-like activity of the Co@N-CNTs catalyst was further explored in O_2 and N_2-saturated solutions in Fig. 6c. A distinct difference value of characteristic absorbance at 652 nm was observed. Compared with the solution under air conditions, the absorption peak intensity of oxTMB increases under the O_2-saturated condition, while the catalytic activity was significantly hindered after saturating with N_2, indicating the vital participation of dissolved O_2 in the oxidation process, as an electron acceptor for TMB oxidation. Consequently, we speculate the mechanism of the catalytic process: at first, the partial positive charge $C^{\delta+}$ sites induced by the doping of electronegative *N* atoms adsorb massive dissolved oxygen onto the surface of the Co@N-CNTs catalyst; then the physically/chemically adsorbed O_2 is transferred to the catalytic active sites (Pyridinic N–Co and pyrrolic N–Co sites) to disintegrate into ROS species ($O_2^{\bullet-}$ and $^{\bullet}OH$); finally, the ROS species activate the oxidation reaction of substrates to emerge the oxidase-like activity. In general, the reduction product of the ROS species is probably H_2O_2. However, the production of H_2O_2 might trigger the peroxidase-mimicking activity of catalysts to accelerate the oxidation of TMB. Therefore, in order to distinguish the effect of peroxidase-

 © 2021 The Author(s). Published by the Royal Society of Chemistry

Open Access Article. Published on 15 December 2021. Downloaded on 5/22/2026 10:09:20 AM.
This article is licensed under a Creative Commons Attribution-NonCommercial 3.0 Unported Licence.

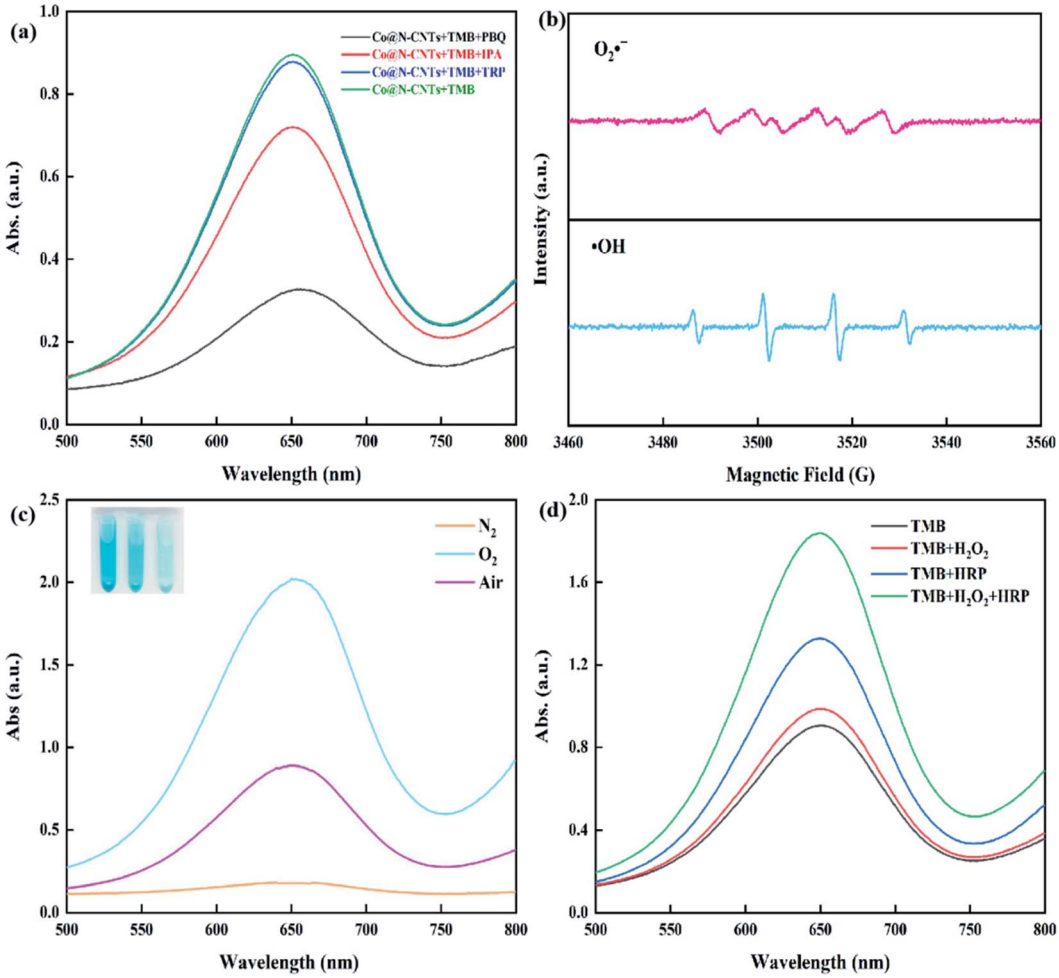

Fig. 6 (a) UV-vis absorption spectra of the Co@N-CNTs catalyst (10 μg mL^{-1}) with TMB (80 μg mL^{-1}) in the presence of different scavengers including PBQ, IPA or TRP, (b) EPR spectra of superoxide anion and hydroxyl radical in the reaction system, (c) UV-vis absorption spectra of TMB in air-saturated, O_2-saturated, and N_2-saturated conditions. (d) UV-vis absorption spectra of the Co@N-CNTs catalyst (10 μg mL^{-1}) with TMB (80 μg mL^{-1}) in the absence or presence of H_2O_2, HRP, or H_2O_2 and HRP.

like catalytic activity, further control experiments were carried out. As exhibited in Fig. 6d, the characteristic absorption peak of oxTMB slightly increases, when horse radish peroxidase (HRP) is added into the reaction solution with the Co@N-CNTs catalyst and TMB, suggesting the production of H_2O_2 after the catalytic reaction. Interestingly, when a dose of H_2O_2 was added into the reaction solution, the intensity of the characteristic absorption peak at 652 nm rises only slightly. On the contrary, when HPR and H_2O_2 are simultaneously filled into the reaction solution, an obvious increase in the characteristic absorption peak was detected. Those results testify that the Co@N-CNTs catalyst just owns weak peroxidase activity; hence, the oxidation of TMB mainly depends on its oxidase-like catalytic activity.

2.3 Determination and colorimetric assay of ascorbic acid

As is well known, AA occupies great importance in many metabolic processes.[42] An abnormal content of AA is generally related to various diseases, for example, deficiency of AA easily induces scurvy, cardiovascular diseases and gingival bleeding[43] while excessive amounts of AA results in diarrhoea, urinary stones and stomach cramps.[44] Hence, a sensitive method for AA detection is highly desired to predict human diseases. In this work, we adopt the oxidase-like activity of the Co@N-CNTs catalyst to develop a technique of AA detection, based on its inhibition and reduction character to reactive oxide species.[45] Different concentrations of AA (0.1–200.0 μM) are injected on the Co@N-CNTs probe test system, and then the photographic images and the absorption spectra were collected after 10 min. As exhibited in Fig. 7a, with the increase in AA concentration, the UV-vis absorption value of the reaction solution obviously decreases. In addition, the colorimetric difference from deep blue to transparently colorless (inset) is identified with naked eyes. Fig. 7b illustrates the dose–response curve between the AA concentration and the absorbance difference (ΔA) ($\Delta A = A_0 - A$, A stands for the absorbance intensity in the presence of AA; A_0 represents the absorbance intensity in the absence of AA at 652 nm). When the concentration of AA is 0.1–10 μM and 10–160 μM, there is a good linear relationship with $R^2 = 0.993$ and $R^2 = 0.998$ (inset), respectively. Using a signal-to-noise ratio of 3 (3σ/

Open Access Article. Published on 15 December 2021. Downloaded on 5/22/2026 10:09:20 AM.
This article is licensed under a Creative Commons Attribution-NonCommercial 3.0 Unported Licence.

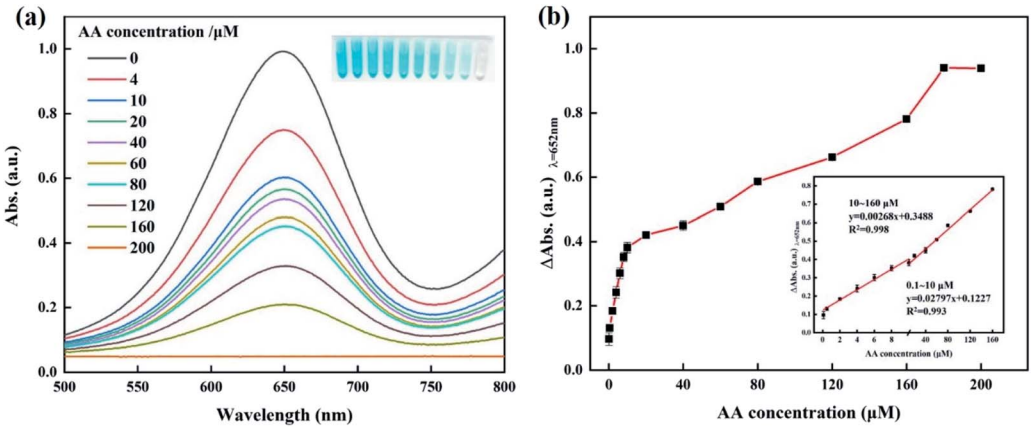

Fig. 7 (a) UV-vis absorption spectra of the reaction system consisting of TMB (80 μg mL^{-1}) and Co@N-CNTs catalyst (10 μg mL^{-1}) in the presence of AA with different concentrations (the inset displays the color changes of reaction solution with the increasing AA concentration). (b) Plots of the absorbance differences at 652 nm *versus* the AA concentrations. Inset is the linear calibration plot corresponding to absorbance against the concentration of AA. The error bars represent the standard deviation values of three measurements.

k), wherein σ stands for the standard deviation of blank samples and k represents the slope of the linear fitting curve, the limit of detection (LOD) was determined to be 0.076 μM. The detection limit is much lower than many previously reported materials, as shown in Table 1, indicating a prominent sensitivity and reliability of this colorimetric method for AA determination. The results indicate that the oxidase-like activity of Co@N-CNTs can be successfully developed into a single-step colorimetric detection approach of AA.

In order to evaluate the anti-interference performance of the colorimetric method, the effect of the possible interfering ions including Na^+, Mg^{2+}, Al^{3+}, Pb^{2+}, Ca^{2+}, Ni^{2+}, Cr^{3+}, Co^{2+}, Zn^{2+}, Ba^{2+}, and K^+ (in 100-fold excess of AA concentration) on AA detection was measured. As depicted in Fig. 8a, through comparing with the absorbance difference (ΔA) of the detection systems containing AA and other interfering substances, it can be found that the presence of interference has no obvious influence on the detection of AA, indicating that the proposed method has good anti-interference ability. In addition, considering the practical application of human serum testing, it is necessary to assess the selectivity of the AA detection platform. Therefore, the selectivity of the proposed colorimetric assay towards AA detection in the presence of multitudinous interfering species such as tryptophan, glycine, histidine, lysine, aspartic acid, serine, threonine, DL-methionine, arginine, valine, and cystine was further investigated by comparing the response of absorbance at 652 nm. Fig. 8b indicates that the absorbance decreased sharply with the blue color disappearance only after addition of AA, while other substances cannot affect the oxidase-like activity of the Co@N-CNTs catalyst. The high sensitivity, anti-interference performance and quick response towards AA endow this sensing platform with excellent specificity to directly detect AA in real samples. Accordingly, we conducted this colorimetric detection approach to measure AA in the human serum (see Fig. S13†). In addition, recovery experiments were executed using the standard addition

Table 1 Comparison of different sensors for AA detection

System	Signal output	Time of analysis	Linear range (μM)	LOD (μM)	References
Cu–Ag/rGO/TMB/H_2O_2	Colorimetry	50 min	5–30	3.6	46
AgNPs/rGOb/GCE	Amperometry	No report	10–800	9.6	47
GSH-AuNCs/H_2O_2/Fe^{2+}	Fluorescence	5 min	5–100	5	48
ClO^-/TMB	Colorimetry	30 s	1–70	0.58	49
CuO nanoneedles/SPEs	Electrochemical	No report	100–8000	88	50
GQDs/H_2O_2/HRP/catechol	Fluorescence	40 min	1.11–300	0.32	51
CoOOH/TMB	Colorimetry	10 min	0.25–60	0.057	52
MnO_2/TMB	Colorimetry	30 min	0.1–20	0.098	53
Ag^+/OPD	Fluorescence	10 min	0.05–1.0, 1.0–40	0.01	54
CdTe QDs	Fluorescence	No report	0–800	3	55
PB NCs/ALP	Colorimetry	15 min	0.4–4.5	0.035	56
Au NCs	Fluorescence	24 h	1.5–10	0.2	57
PNCQDs/Cr(VI)	Fluorescence	72 h	5–200	1.35	58
Co@N-CNTs/TMB	Colorimetry	10 min	0.1–10, 10–160	0.076	This work

 © 2021 The Author(s). Published by the Royal Society of Chemistry

Open Access Article. Published on 15 December 2021. Downloaded on 5/22/2026 10:09:20 AM.
This article is licensed under a Creative Commons Attribution-NonCommercial 3.0 Unported Licence.

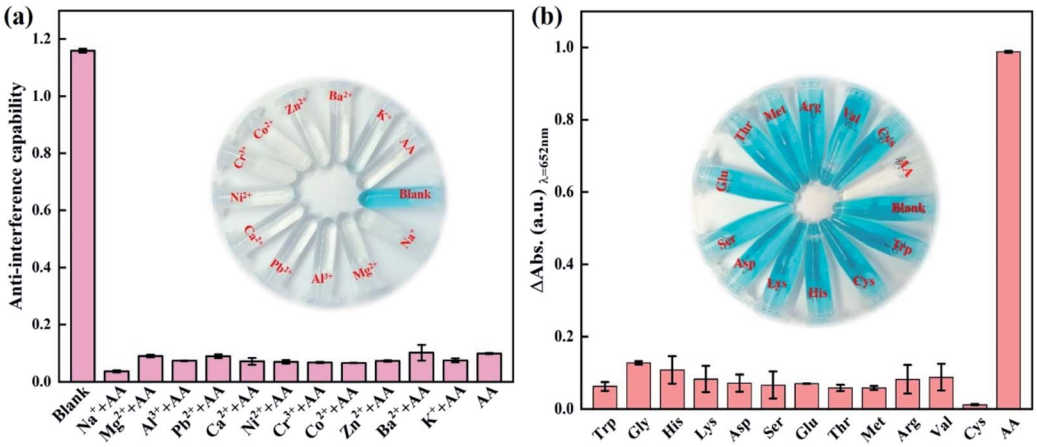

Fig. 8 (a) Anti-interference ability of this detection platform for AA assay towards coexisting interference substances including Na^+, Mg^{2+}, Al^{3+}, Pb^{2+}, Ca^{2+}, Ni^{2+}, Cr^{3+}, Co^{2+}, Zn^{2+}, Ba^{2+}, K^+ and AA. (b) Selectivity of this detection platform for AA assay. From left to right: tryptophan, glycine, histidine, lysine, aspartic acid, serine, threonine, methionine, arginine, valine, cystine, and ascorbic acid (the concentration of the substance in the system: 80 μg m^{-1} TMB; 10 μg mL^{-1} Co@N-CNTs catalyst; 160 μM AA; 20 mM interference ions). The error bars represent the standard deviation values of three measurements. The insets are the corresponding photographs of color changes.

Table 2 Recoveries of the determination of AA in human serum samples using the proposed sensor

Sample	Added	Found (μM)	Recovery (%)	RSD (%, $n = 3$)
Human serum	0	0.049	—	0.1414
1	5	5.45	109.10	1.6971
2	10	9.68	96.80	0.6364
3	15	14.74	98.27	1.5556
4	20	19.89	99.45	2.1213
5	25	24.99	99.96	0.0707

method, where different concentrations of AA were spiked in human serum samples for analysis. In order to reduce the stochastic error, an average value was obtained by measuring three parallel trials. As exhibited in Table 2, satisfactory recoveries of 96.8–109.1% with a relative standard deviation (RSD) of three replicate detections for each sample lower than 3% were obtained. The above-mentioned results confirm the potential feasibility and wide application prospect of the as-proposed colorimetric method for AA detection in real samples.

3. Conclusion

In summary, a novel Co@N-CNTs hybrid catalyst with oxidase-like activity has been successfully designed by the synergy strategies of nanostructural engineering, carbon coating and N doping. In this hybrid catalyst, the N-doped carbon nanotubes embedded with Co nanoparticles were randomly anchored on the hollow N-doped dodecahedron carbon skeleton. The special structure offers open channels and huge surface area to expedite the mass/electron transfer and to expose catalytically active sites. Wrapping Co nanoparticles in carbon nanotubes effectively prevents the agglomeration of nanoparticles by confined effects; meanwhile, it avoids the inactivation of active sites due to direct exposure to the substrate solution, thereby guaranteeing the excellent stability and satisfactory catalytic activity. N-doping triggers the local charge transfer to generate partial positive charge $C^{\delta+}$ sites on adjacent carbon, which is conductive to trapping the dissolved oxygen and promoting the catalytic process. In addition, the synergistic interfacial effect between Co nanoparticles and N-doped carbon nanotubes creates an interfacial electric field, which accelerates the electron transfer from the substrate to the catalyst. Consequently, the Co@N-CNTs hybrid catalyst as a mimic enzyme presents glorious oxidase-like catalytic property, which can covert colorless TMB to blue ox-TMB. The Co@N-CNTs hybrid catalyst can be used for the sensitive colorimetric detection of AA with a detection limit of 0.076 μM, based on the inhibitory effect of AA on its mimic enzyme activity. It can be rationally anticipated that this study proposes a universal method for the preparation of hybrid catalysts with prominent oxidase-like activity for further applications, such as biosensing, medical diagnosis, and environment monitoring.

Ethical statement

All animal procedures were performed in accordance with the Guideline for Care and Use of Laboratory Animals of Chongqing Normal University and approved by the Animal Ethics Committee of Chongqing Normal University. Serum samples were collected from the volunteers of the Affiliated Hospital of Chongqing Medical University and informed consent was obtained from all human subjects.

Conflicts of interest

The authors declare no competing financial interest.

Open Access Article. Published on 15 December 2021. Downloaded on 5/22/2026 10:09:20 AM. This article is licensed under a Creative Commons Attribution-NonCommercial 3.0 Unported Licence.

Acknowledgements

This work was supported by the Science and Technology Research Program of Chongqing Municipal Education Commission (KJZD-K201900503), Achievement Transfer Program of Institutions of Higher Education in Chongqing (No. KJZH17112), Chongqing Research Program of Basic Research and Frontier Technology (cstc2019jcyj-msxmX0523), Innovation and Entrepreneurship Team of Inorganic Optoelectronic Functional Materials for Chongqing Yingcai (No. cstc2021ycjh-bgzxm0131), the Chongqing Innovation Research Group Project (No. CXQT21015), Doctor Start/Talent Introduction Program of Chongqing Normal University (No. 02060404/2020009000321) and Postgraduate Innovation Project of Chongqing Normal University (No. CYS21281). W. Fu was sponsored by the Chongqing Talent Program (Leading talent).

References

1 L. Gao, J. Zhuang, L. Nie, J. Zhang, Y. Zhang, N. Gu, T. Wang, J. Feng, D. Yang, S. Perrett and X. Yan, *Nat. Nanotechnol.*, 2007, **2**, 577–583.
2 J. Lian, Y. He, N. Li, P. Liu, Z. Liu and Q. Liu, *Inorg. Chem.*, 2021, **60**, 1893–1901.
3 H. Chen, C. Yuan, X. Yang, X. Cheng, A. A. Elzatahry, A. Alghamdi, J. Su, X. He and Y. Deng, *ACS Appl. Nano Mater.*, 2020, **3**, 4586–4598.
4 N. Kotov, *Science*, 2010, **330**, 188–189.
5 S. Cai, C. Qi, Y. Li, Q. Han, R. Yang and C. Wang, *J. Mater. Chem. B*, 2016, **4**, 1869–1877.
6 M. Gao, X. Lu, M. Chi, S. Chen and C. Wang, *Inorg. Chem. Front.*, 2017, **4**, 1862–1869.
7 H. Zhang, T. Watanabe, M. Okumura, M. Haruta and N. Toshima, *Nat. Mater.*, 2012, **11**, 49–52.
8 S. Zheng, X. Li, B. Yan, Q. Hu, Y. Xu, X. Xiao, H. Xue and H. Pang, *Adv. Energy Mater.*, 2017, **7**, 1602733.
9 H. Lim, Y. Ju and J. Kim, *Anal. Chem.*, 2016, **88**, 4751–4758.
10 Y. Hu, X. J. Gao, Y. Zhu, F. Muhammad, S. Tan, W. Cao, S. Lin, Z. Jin, X. Gao and H. Wei, *Chem. Mater.*, 2018, **30**, 6431–6439.
11 T. Zhang, Y. Xing, Y. Song, Y. Gu, X. Yan, N. Lu, H. Liu, Z. Xu, H. Xu, Z. Zhang and M. Yang, *Anal. Chem.*, 2019, **91**, 10589–10595.
12 J. Mou, X. Xu, F. Zhang, J. Xia and Z. Wang, *ACS Appl. Bio Mater.*, 2020, **3**, 664–672.
13 S. Huang, F. Ge, J. Yan, H. Li, X. Zhu, Y. Xu, H. Xu and H. Li, *J. Energy Chem.*, 2021, **54**, 403–413.
14 K. Fan, J. Xi, L. Fan, P. Wang, C. Zhu, Y. Tang, X. Xu, M. Liang, B. Jiang, X. Yan and L. Gao, *Nat. Commun.*, 2018, **9**, 1440.
15 H. Fu, K. Huang, G. Yang, Y. Cao, H. Wang, F. Peng, Q. Wang and H. Yu, *ACS Catal.*, 2020, **10**, 129–137.
16 N. Song, F. Ma, Y. Zhu, S. Chen, C. Wang and X. Lu, *ACS Sustainable Chem. Eng.*, 2018, **6**, 16766–16776.
17 Y. Qiu, C. Yang, J. Huo and Z. Liu, *J. Mol. Catal. A: Chem.*, 2016, **424**, 276–282.
18 Y. Zhuang, X. Zhang, Q. Chen, S. Li, H. Cao and Y. Huang, *Mater. Sci. Eng. C*, 2019, **94**, 858–866.
19 O. Arrigoni and M. C. De Tullio, *Biochim. Biophys. Acta*, 2002, **1569**, 1–9.
20 A. Meister, *J. Biol. Chem.*, 1994, **269**, 9397–9400.
21 H. Wang, G. Pu, S. Devaramani, Y. Wang, Z. Yang, L. Li, X. Ma and X. Lu, *Anal. Chem.*, 2018, **90**, 4871–4877.
22 C. Wang, C. Pan, Z. Wei, X. Wei, F. Yang and L. Mao, *Anal. Chim. Acta*, 2020, **1100**, 191–199.
23 A. G. Frenich, M. E. H. Torres, A. B. Vega, J. L. M. Vidal and P. P. Bolaños, *J. Agric. Food Chem.*, 2005, **53**, 7371–7376.
24 Q. Zhu, D. Dong, X. Zheng, H. Song, X. Zhao, H. Chen and X. Chen, *RSC Adv.*, 2016, **6**, 25047–25055.
25 K. S. Park, Z. Ni, A. P. Côté, J. Y. Choi, R. Huang, F. J. Uribe-Romo, H. K. Chae, M. O'Keeffe and O. M. Yaghi, *Proc. Natl. Acad. Sci. U. S. A.*, 2006, **103**, 10186–10191.
26 R. Banerjee, A. Phan, B. Wang, C. Knobler, H. Furukawa, M. O'Keeffe and O. M. Yaghi, *Sciences*, 2008, **319**, 939–943.
27 F. Tf and J. L. Koenig, *J. Chem. Phys.*, 1970, **53**, 1126–1130.
28 K. G. Neoh, E. T. Kang and K. L. Tan, *J. Phys. Chem. B*, 1997, **101**, 726–731.
29 H. C. van der Mei, J. de Vries and H. J. Busscher, *Surf. Sci. Rep.*, 2000, **39**, 1–24.
30 S. J. Guo, S. Zhang, L. H. Wu and S. H. Sun, *Angew. Chem., Int. Ed.*, 2012, **51**, 11770–11773.
31 X. Zhang, R. Liu, Y. Zang, G. Liu, G. Wang, Y. Zhang, H. Zhang and H. Zhao, *Chem. Commun.*, 2016, **52**, 5946–5949.
32 Q. He, Q. Li, S. Khene, X. Ren, F. E. López-Suárez, D. Lozano-Castelló, A. Bueno-López and G. Wu, *J. Phys. Chem. C*, 2013, **117**, 8697–8707.
33 B. Lindsay, M. L. Abel and J. F. Watts, *Carbon*, 2007, **45**, 2433–2444.
34 G. Wu, K. L. More, C. M. Johnston and P. Zelenay, *Science*, 2011, **332**, 443–447.
35 G. Yang, J. Liu, M. Zhou, J. Bai and X. Bo, *ACS Sustainable Chem. Eng.*, 2020, **8**, 11947–11955.
36 K. Olsen, K. R. Kristiansen and L. H. Skibsted, *Food Chem.*, 2003, **80**, 255–260.
37 P. Dance, E. Edwards, T. Asano, M. V. Basilevsky and N. Weinberg, *Can. J. Chem.*, 2010, **88**, 839–848.
38 Y. Li, P. Zhang, W. Fu, L. Chen, S. Wu, Y. Long and Y. Wang, *Analyst*, 2019, **144**, 5479–5485.
39 M. Wang, X. Zhou, S. Wang, X. Xie, Y. Wang and X. Su, *Anal. Chem.*, 2021, **93**, 3130–3137.
40 W. Su, J. Chen, L. Wu, X. Wang, X. Wang and X. Fu, *Appl. Catal., B*, 2008, **77**, 264–271.
41 Y. Wu, J. Wu, L. Jiao, W. Xu, H. Wang, X. Wei, W. Gu, G. Ren, N. Zhang, Q. Zhang, L. Huang, L. Gu and C. Zhu, *Anal. Chem.*, 2020, **92**, 3373–3379.
42 F. Li, Y. Yu, F. Xiao, H. Liang, C. Liu, P. Fan and S. Yang, *Luminescence*, 2020, **35**, 1084–1091.
43 L. Liping, Y. Luo, Q. Chen, Q. Lai and Q. Zheng, *Luminescence*, 2020, **35**, 542–549.
44 D. Yue, D. Zhao, J. Zhang, L. Zhang, K. Jiang, X. Zhang, Y. Cui, Y. Yang, B. Chen and G. Qian, *Chem. Commun.*, 2017, **53**, 11221–11224.

 © 2021 The Author(s). Published by the Royal Society of Chemistry

Open Access Article. Published on 15 December 2021. Downloaded on 5/22/2026 10:09:20 AM.
This article is licensed under a Creative Commons Attribution-NonCommercial 3.0 Unported Licence.

45 H. Sun, Y. Zhou, J. Ren and X. Qu, *Angew. Chem., Int. Ed.*, 2018, **57**, 9224–9237.
46 G. Darabdhara, B. Sharma, M. R. Das, R. Boukherroub and S. Szunerits, *Sens. Actuators, B*, 2017, **238**, 842–851.
47 B. Kaur, T. Pandiyan, B. Satpati and R. Srivastava, *Colloids Surf., B*, 2013, **111**, 97–106.
48 L. Hu, L. Deng, S. Alsaiari, D. Zhang and N. Khashab, *Anal. Chem.*, 2014, **86**, 4989–4994.
49 C. Mu, H. Lu, J. Bao and Q. Zhang, *Spectrochim. Acta, Part A*, 2018, **201**, 61–66.
50 B. Mahmoud, M. Khairy, F. Rashwan, C. Foster and C. Banks, *RSC Adv.*, 2016, **6**, 14474–14482.
51 H. Liu, W. Na, Z. Liu, X. Chen and X. Su, *Biosens. Bioelectron.*, 2017, **92**, 229–233.
52 Q. Nie, Q. Cai, H. Xu, S. Qiao and Z. Li, *Anal. Methods*, 2018, **10**, 2623–2628.
53 P. Chen, H. Zhong, X. Wang, C. Shao, S. Zhi, X.-r. Li and C. Wei, *Anal. Methods*, 2019, **11**, 1469–1474.
54 S. Zhu, C. Lei, Y. Gao, J. Sun, H. Peng, H. Gao, R. Zhang, R. Wang, X.-e. Zhao and H. Wang, *New J. Chem.*, 2018, **42**, 3851–3856.
55 P. Chen, S. Yan, E. Sawyer, B.-w. Ying, X. Wei, Z. Wu and J. Geng, *Analyst*, 2019, **144**, 1147–1152.
56 T. Wu, W. Hou, Z. Ma, M. Liu, X. Liu, Y. Zhang and S. Yao, *Microchim. Acta*, 2019, **186**, 123.
57 X. Wang, P. Wu, X. Hou and Y. Lv, *Analyst*, 2013, **138**, 229–233.
58 X. Gong, Y. Liu, Z. Yang, S. Shuang, Z. Zhang and C. Dong, *Anal. Chim. Acta*, 2017, **968**, 85–96.